ACS Catalysis

pubs.acs.org/acscatalysis

Research Article

Developing Efficient Suzuki Cross-Coupling Catalysts by Doping Palladium Clusters with Silver

Turbasu Sengupta, Dinesh Bista, and Shiv N. Khanna*

Cite This: *ACS Catal.* 2021, 11, 11459–11468

Read Online

ACCESS | Metrics & More | Article Recommendations | Supporting Information

ABSTRACT: It is shown that doping of a Pd cluster by Ag atoms can provide an efficient catalyst for the Suzuki–Miyaura cross-coupling reactions. We demonstrate this intriguing possibility by considering a model reaction involving bromobenzene and phenylboronic acid as reagents where the reaction involves oxidation, transmetallation, and reduction steps. We have examined the reaction barriers of all three steps for a conventional ligated Pd catalyst, a nearly icosahedral Pd_{13} cluster, and a monosilver-doped $Pd_{12}Ag$ cluster using gradient-corrected density functional theory. It is observed that the reaction carried out on the Pd sites adjacent to an Ag atom in a $Pd_{12}Ag$ cluster shows substantially lower barriers for the oxidation and reduction steps compared to the conventional ligated Pd catalyst and the pure Pd_{13} cluster. A detailed analysis indicates that the Ag site donates charge to the neighboring Pd site. While such a donation may have been expected to reduce the barrier for the oxidative step, the lowering of the barrier for the reduction step indicates that the respective sites not only act as a donor but can also serve as an acceptor for the reduction step. Furthermore, because of the differential donor–acceptor characteristic of the Ag and Pd atoms, it is observed that the barrier heights of the redox steps are primarily dependent on the chosen active site. The calculated results show that by altering the atom (Ag or Pd) at the active site of the reaction, the activation energies of the redox steps can either be reduced or increased. This shows that the active sites of a bimetallic cluster-like $Pd_{12}Ag$ can be utilized to control the barrier heights of suitable chemical reactions. The relative trend of the barrier heights for both clusters is also observed to be predictable by the conceptual density functional theory. Previous studies in our group have indicated that the reaction barriers for Pd_n clusters can be lowered by supporting them on reduced graphene. We, therefore, propose that silver-doped Pd_n clusters may provide an even better catalyst.

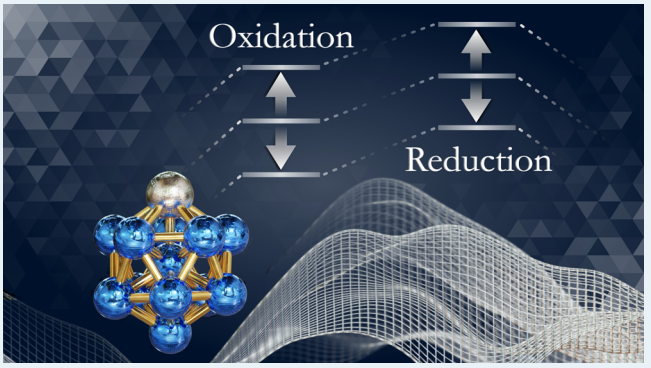

KEYWORDS: *metal clusters, cluster chemistry, catalysts, cross-coupling reaction, palladium, doping*

1. INTRODUCTION

The increasing demand for inexpensive, efficient, and environmentally safe chemical processes has stimulated the development of novel catalysts. Diverse materials employed as catalysts include metal oxides, metal complexes, and organic and inorganic polymers, as well as biocatalysts and photocatalysts.[1−7] Because of the metastability of free clusters, such reactions are usually catalyzed by clusters on inert supports or by ligated clusters.[8−11] The ligand protects the cluster core, whereas the surface reduces mobility and inhibits coalescence. Within the list of the notable chemical reactions where metal clusters are frequently used as a catalyst, the C–C cross-coupling reaction deserves a noteworthy mention.[12−15] Here, two organic fragments are combined together using a suitable catalyst.[13,14] One of the most important catalysts for such reactions is palladium clusters/nanoparticles. The reactions are usually carried out under homogeneous conditions, utilizing ligands to enhance activity and selectivity. However, the process leads to residual palladium in the solution that contaminates the reaction product.[16−19] Because palladium compounds can be highly toxic, this is a major problem in pharmaceutical applications where this chemistry is extensively employed.[20,21] Also the inability to recycle the metal results in a significant cost component in pharmaceutical applications. The development of supported heterogeneous catalysts that could reduce/eliminate leaching and sintering, could enhance the performance, and could be recycled would be a giant step in lowering the cost of the synthesis of chemicals and drugs.

It was recently discovered that palladium clusters supported on the defects of reduced graphene oxide lead to a high-

Received: May 7, 2021
Revised: July 29, 2021
Published: August 31, 2021

performance heterogeneous catalyst.[16,17,22] Experimental studies focused on a Suzuki−Miyaura (SM) reaction[23,24] using 4-bromobenzoic acid and phenylboronic acid as reagents. The reaction involves a three-step pathway involving oxidative addition, transmetallation, and reductive elimination. In these studies, Pd nanoparticles supported on reduced graphene oxide were synthesized by impregnating a Pd precursor with graphene oxide followed by hydrazine and microwave heating coreduction. Structural investigations of the resulting catalyst using STM and other probes indicated that such a process generates vacancy defect sites/voids on the reduced graphene sheet with Pd_n particles strongly bound to these vacancies/voids. The resulting catalysts exhibited remarkable catalytic activity compared to other support systems with turnover frequencies (TOFs) that were orders of magnitude higher than those of other catalysts. Furthermore, negligible metal leaching was observed when these materials were used in cross-coupling reactions, and the catalysts could be recovered and recycled several times without any significant loss of catalytic activity. The enhanced catalytic activity, along with the apparently strong binding of Pd clusters to the defected graphene support, suggested that an electronic interaction occurred between Pd nanoclusters and graphene. Theoretical studies[16,22] indicated that the enhanced activity could be related to the graphene acting as a reservoir of electrons that donated/accepted charge for the oxidation and reduction steps, thereby lowering the barrier of the various steps of cross-coupling reactions. While the discovery of supported palladium clusters represents a significant advancement, it raises the question as to whether there are any other ways to enhance the activity and lower the cost by replacing Pd with another element. In particular, is there an alternative approach to control the donor/acceptor characteristics of a local Pd site?

The objective of this paper is to propose an alternative approach to enhance the catalytic activity of Pd clusters using a mixed/bimetallic cluster where one or more of the surface sites are replaced by Ag atoms. Our choice of Ag is motivated by its electron configuration of a filled 4d-shell and a single 5s electron. Our idea was to explore if such an atom with a filled d-shell and an unfilled s-level could act as an effective donor or acceptor, thus enhancing the activity of the neighboring Pd sites. Because Ag is far less expensive than Pd, such a cluster would enhance activity at a lower cost. We investigate this interesting prospect by considering the reaction pathways of the SM cross coupling[23,24] reaction on the distorted icosahedral Pd_{13} and monosilver-doped $Pd_{12}Ag$ cluster. An analysis of the cluster surface reveals that the dopant Ag atom perturbs the near-symmetrical charge distribution on the surface and thereby creates sites with differential chemical reactivity. Relative comparison of the activation energies with the Pd_{13} cluster and the $Pd(PPh_3)_2$ catalysts shows that by carrying out the reaction on the Pd sites, which are nearby to the Ag dopant, the barrier heights of the redox steps can be significantly reduced. Therefore, the selected Pd sites on $Pd_{12}Ag$ act as a much better catalyst compared to either Pd_{13} or $Pd(PPh_3)_2$ in terms of activation energy. In addition, by altering the atom (Ag or Pd) at the active site of the SM reaction, the barrier heights for the redox steps can either be increased or reduced, thus providing a way to control the barrier heights. The calculated barrier heights of the $Pd_{12}Ag$ and Pd_{13} clusters are also found to be consistent with the computed local reactivity descriptors.[25−27] The interesting correlation between the computed reactivity descriptors and the barrier heights is significant because it provides an opportunity to predict the catalytic performance of the individual sites on the cluster. The relative trends of the energy barriers are also observed to be spin-independent because it is noticed that the energy barriers of other spin states are also altered in a similar manner. We would like to add that the current work is a first step toward generating a heterogeneous catalyst that outperforms the current catalyst consisting of Pd_n clusters bound to defects on graphene.[16,17] We propose that Pd_xAg_y clusters supported on reduced graphene may provide a less expensive and more effective catalyst for the cross-coupling reaction.

2. METHODS

All the results reported here are based on the density functional theory (DFT) methodology. The calculations are performed using the Amsterdam Density Functional (ADF) program.[28] The gradient-corrected Perdew, Burke, and Ernzerhof (PBE) exchange-correlation functional was used for all calculations.[29] The Slater-type triple ζ basis set with two polarization functions (TZ2P) and with a large frozen electron core was used for all the elements.[30,31] To account for the relativistic effects for the heavy elements, the zero-order regular approximation (ZORA)[32,33] was included as well. The geometry optimizations for all the reported structures were carried out using the Hessian-based quasi-Newton method without any symmetry constraints.[34] The analytical frequency calculation[35,36] was performed for all the optimized structures, and it was checked that all the normal modes of the energetical minima structures are real-positive, whereas the transition states are first-order saddle points with only one imaginary frequency of appropriate magnitude. To ensure the accuracy of the reported transition states, intrinsic reaction coordinate (IRC) calculations[37] were performed for selected transition states. The IRC calculations verified that the respective transition states are connected to the reported minima at the left and the right-hand sides of the transition state. The rate constants of the individual steps are calculated using the Eyring−Polanyi[38,39] equation, whereas the TOFs of the catalytic cycles are estimated by the AUTOF[40] (excel version) utilizing the energetic span model (ESM).[41−45] The spin contamination values are also checked for all the optimized structures, and no significant deviation was found for any of them. To determine the global minima of each structure, a wide range of spin multiplicities were examined, and only the lowest energy structures were chosen for all cases. The zero-point energy correction is included in the energies of all the species reported in the reaction pathway. The conceptual DFT calculations were evaluated by the frontier molecular orbital (FMO) approximation with degeneracy correction as implemented in the ADF.[25] The numerical values of the condensed descriptors are obtained by a quantum theory of atoms and molecules (QTAIM)[46] partition scheme. The three-dimensional isosurface representations of the Fukui functions[26] are generated by simple arithmetic operation using the total electron density of the neutral, cationic, and anionic species at the equilibrium geometry. The average binding energies (ΔE_b) for the clusters are calculated as,

For the Pd_{13} cluster:

$$\frac{n \cdot E_{Pd} - E_{Pd_n}}{n} \quad (1)$$

https://doi.org/10.1021/acscatal.1c02083
ACS Catal. 2021, 11, 11459−11468

For the $Pd_{12}Ag$ cluster:

$$\frac{E_{Ag} + (n-1)\cdot E_{Pd} - E_{Pd_{(n-1)}Ag}}{n} \quad (2)$$

where E_{Pd} and E_{Ag} are the energies of the ground state (GS) of the respective isolated atoms. E_{Pd_n} and $E_{Pd_{(n-1)}Ag}$ are the energies of the GS clusters for n = 13. To calculate the Hirshfeld-I charge[47] and average local ionization energy[48,49] (ALIE, $\bar{I}(r)$), the Gaussian09 package[50] was used in combination with Multiwfn.[51] The ALIE is defined as,

$$\bar{I}(r) = \frac{\sum_i \rho_i(r)|\varepsilon_i|}{\rho(r)} \quad (3)$$

$\rho_i(r)$ and $|\varepsilon_i|$ are the electron density and energy of the ith molecular orbital (MO) and $\rho(r)$ is the total electron density, respectively. The optimization and energy evaluation in the Gaussian09 package[50] were performed using the PBE/def2-SVP[52,53] level of theory.

3. RESULTS AND DISCUSSION

3.1. Effect of Silver Atom Doping on the Electronic Properties of Palladium Clusters. To investigate the electronic properties of the icosahedral Pd_{13} and $Pd_{12}Ag$ clusters, we have first optimized the GS structures of both. For the present work, we have chosen the nearly icosahedral Pd_{13} isomer because it is experimentally[16,22,54] observed that the Pd_{13} cluster adopts a distorted icosahedral shape when deposited on chemical supports, which are commonly used for catalytic purposes. The optimized GS of the two clusters with interatomic distances (in Å) is shown in Figure 1a. The GS spin multiplicity (M = $2S$ + 1) of the nearly icosahedral Pd_{13} cluster was found to be 9, whereas the spin multiplicity for the lowest energy structure of $Pd_{12}Ag$ is calculated to be 8. The relative energies of other spin multiplicities are provided in Table S1 (Supporting Information). Because of the inclusion of the Ag dopant at the vertex of the icosahedra, minor structural changes are noticed. The Pd−Ag bond length is also found to be within a similar range to Pd−Pd, as shown in Figure 1a. The removal energy of the Ag atom (2.38 eV) from the $Pd_{12}Ag$ cluster is calculated to be lower than the removal energy of a Pd atom (2.72 eV) from the Pd_{13} cluster. Despite the difference, the average binding energies (ΔE_b) of both clusters are very close. The ΔE_b values for the Pd_{13} cluster and $Pd_{12}Ag$ cluster are calculated as 2.05 and 2.03 eV, respectively. The major difference is observed in the charge distribution of both clusters. Figure 1b,c shows the net total Voronoi (NTV)[55] and Hirshfeld-I[47,50,51] charges of Pd_{13} and $Pd_{12}Ag$ clusters, respectively. It is observed that compared to Pd_{13}, the $Pd_{12}Ag$ cluster shows relatively asymmetric charge distribution on the surface. During doping, the Ag atom on the surface has acted as a donor and hence is positively charged, whereas the charges on the majority of Pd sites are negative. It is also interesting to note that the Pd atoms, which are in close proximity to the dopant Ag, show higher negative charges than the rest of the Pd atoms. Despite the high basis set dependency[56,57] of Mulliken population analysis,[58] the Mulliken charges also show a similar trend. Investigation of spin densities of both clusters shows that the spin densities are localized only on the Pd atoms. The Mulliken charge and the spin density data are included in the Supporting Information (Table S2 and Figure S1). Based on the computed charges, it

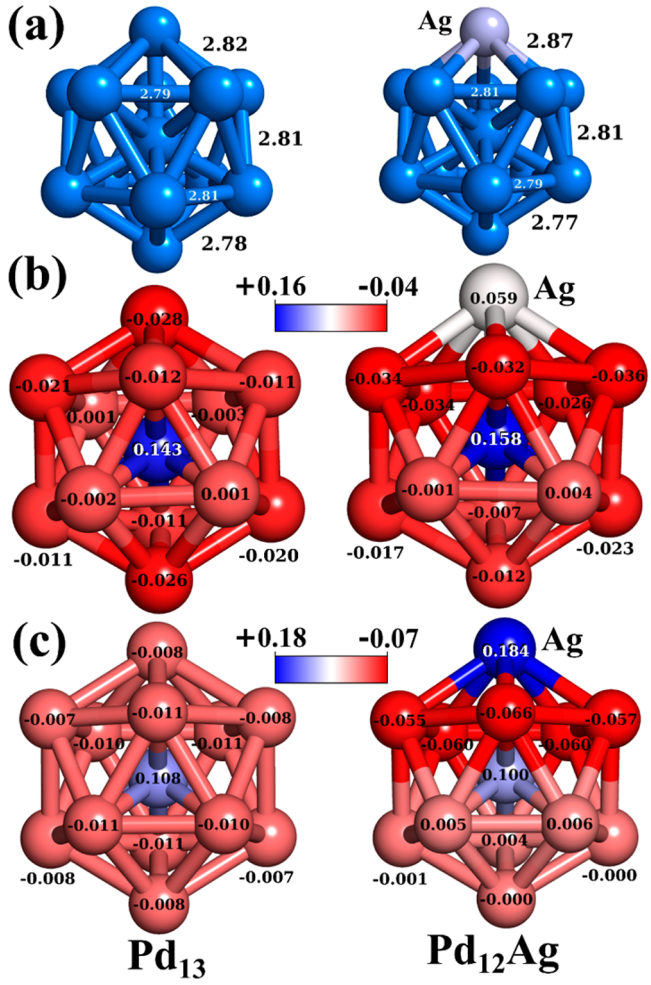

Figure 1. (a) Optimized GS structures (distances are in Å), (b) net total Voronoi (NTV) charges, and (c) Hirshfeld-I charges of GS Pd_{13} and $Pd_{12}Ag$ clusters.

can be argued that the electron-poor Ag atom on the surface primarily acts as a Lewis acid (electrophile), whereas the electron-rich Pd atoms act as Lewis bases (nucleophile). In other words, the Ag atom will be more susceptible for an attack by a nucleophilic reagent while the Pd atoms which are in close vicinity to the dopant Ag will favor an electrophilic attack as they are more negatively charged than the rest.

To further quantify the Lewis acid−base characteristics, we have calculated the average local ionization energy[48,49] (ALIE, $\bar{I}(r)$) and plotted the Fukui[26] isosurfaces for the GS of the Pd_{13} and $Pd_{12}Ag$ clusters (Figure 2). The ALIE identifies the location of weakly bounded electrons on the cluster surface, and the locations of the minima indicate the preferential sites for the electrophilic attack. As shown in Figure 2a, the local minima (marked by green dots) of ALIE are uniformly distributed on the surface of Pd_{13}. On the contrary, in the case of $Pd_{12}Ag$, the minima are observed to be localized only near the Pd atoms. The color-mapped isosurface also shows the same (ALIE data are provided in Table S3 of the Supporting Information). The relatively lower magnitude of ALIE in the proximity of Pd atoms in the $Pd_{12}Ag$ cluster further indicates that the Pd sites are more susceptible to an electrophilic attack compared to Ag. The computed isosurfaces of the Fukui (f^+ and f^-) function also show a nice agreement with the ALIE values. As shown in Figure 2b,c, the positive part of f^+ is

https://doi.org/10.1021/acscatal.1c02083
ACS Catal. 2021, 11, 11459−11468

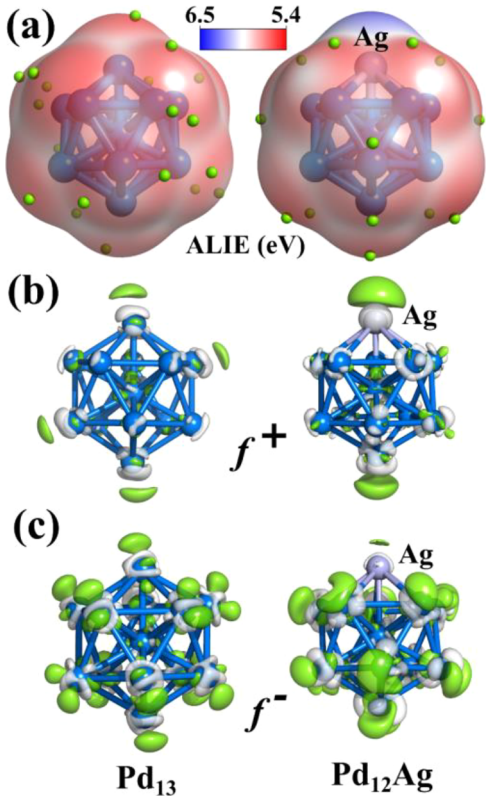

Figure 2. (a) ALIE and the isosurface (isovalue = 0.002) representation of (b) Fukui f^+ and (c) Fukui f^- function for the GS Pd_{13} and $Pd_{12}Ag$ cluster. The positive lobes are colored green, whereas the negative lobes are marked by white color.

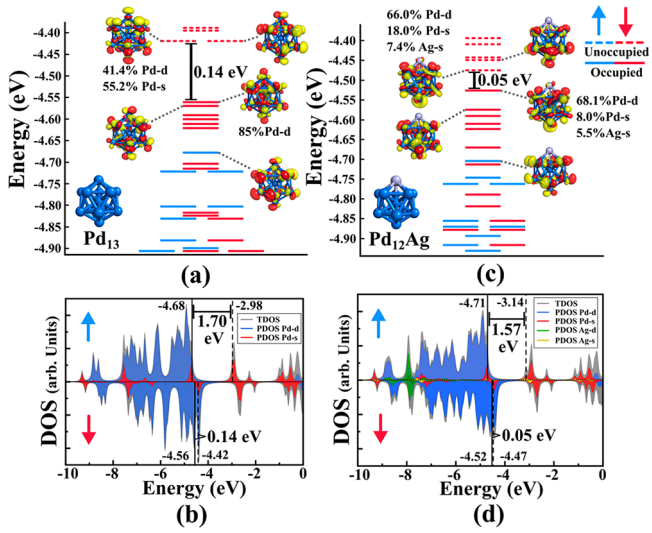

Figure 3. MO diagram and density of states (DOS) plots for the GS Pd_{13} (a, b) and $Pd_{12}Ag$ (c, d) cluster, respectively. The isosurfaces (isovalue = 0.03) of a few important MOs are also shown.

localized on the dopant Ag of the $Pd_{12}Ag$ cluster, whereas most of the positive region of f^- is localized on the Pd atoms. To further test the donor characteristics of the Pd sites, we calculated the binding energy of a Cl atom to the Pd atoms adjacent to the Ag atom. The Cl atom shows 0.06 eV higher binding energy with the Pd atoms in the $Pd_{12}Ag$ cluster compared to Pd_{13} (see Figure S2 of the Supporting Information). This observation also indicates that the respective Pd atoms in the $Pd_{12}Ag$ cluster are more susceptible to an electrophilic attack than the Pd atoms in Pd_{13}.

To analyze the electronic structures of Pd_{13} and $Pd_{12}Ag$ clusters, we now consider the electronic states. The MO diagram and the density of states (DOS) plot of the two clusters are shown in Figure 3a−d. The $HOMO_\uparrow$−$LUMO_\uparrow$ gap for the Pd_{13} cluster is calculated as 1.70 eV, whereas the $HOMO_\downarrow$−$LUMO_\downarrow$ gap is 0.14 eV. The valence region is dominated by ↓ spin orbitals, and the $HOMO_\uparrow$ orbital lies much lower in energy. Hence, the unusually low $HOMO_\downarrow$−$LUMO_\downarrow$ gap (0.14 eV) can be considered as the reason for the observed high reactivity of the icosahedral Pd_{13} cluster.[59] The MO composition analysis reveals that the $HOMO_\downarrow$ of Pd_{13} is mostly composed of Pd d orbitals, whereas the $LUMO_\downarrow$ shows a hybrid composition of d and s orbitals of Pd atoms. The introduction of Ag dopants within the icosahedron shows minor changes in the MO and DOS diagram, especially near the valence region. The $HOMO_\downarrow$ for the $Pd_{12}Ag$ cluster shows the dominant contribution of the Pd d orbitals along with minor s contribution from Pd and Ag. The composition of $LUMO_\downarrow$ has remained like Pd_{13}, except that the contribution from the s orbital of Pd has reduced significantly, and minor contamination from the s orbital of Ag is noticed. Compared to the GS of the Pd_{13} cluster, the energies of the $HOMO_\downarrow$ and $LUMO_\downarrow$ orbitals of the $Pd_{12}Ag$ cluster have marginally altered, resulting in a small lowering in the $HOMO_\downarrow$−$LUMO_\downarrow$ gap (0.05 eV). Likewise, the $HOMO_\uparrow$−$LUMO_\uparrow$ gap is reduced to 1.57 eV. Thus, it is expected that, akin to the Pd_{13} cluster, the frontier orbitals from the ↓ spin will have a dominant effect in controlling the reactivity of the $Pd_{12}Ag$ cluster. We have also recalculated the HOMO−LUMO gap using a few selected meta-generalized gradient approximation (meta-GGA) and hybrid DFT functionals and observed that the meta-GGA results are very similar as reported herewith (Table S4 of the Supporting Information). On the contrary, the HOMO−LUMO gaps for the hybrid calculations are found to be larger than those obtained from GGA-PBE; however, the relative trend remained the same irrespective of the DFT functional used for the calculations. The DOS plots in Figure 3b,d draw a similar conclusion to the HOMO and LUMO. The d orbitals of Ag atoms are buried at a lower energy (∼−8.0 eV), and both the $HOMO_\downarrow$ and $LUMO_\downarrow$ orbitals show a dominant contribution from Pd atoms with some minor contamination from the s orbitals of the Ag atom. It is important to mention that although the overall DOS diagrams of the two clusters may look similar, if one compares the projected DOS of only the dopant Ag atom ($Pd_{12}Ag$) to one of the Pd atoms (Pd_{13}) at the vertices, there will be much bigger differences (see Figure S3 of the Supporting Information) especially in the projected DOS regions of the d orbitals. For the present systems, such comparison is more relevant because it is analogous to the observed difference in the charge distribution between the vertex Ag and Pd atoms.

From the reported results, it is now evident that all the calculated results show that the overall electronic structure of the GS $Pd_{12}Ag$ is mostly similar to that of the Pd_{13} cluster. The MO and DOS diagrams are marked only by a handful of minor alterations. The charge[47,55] distribution, ALIE,[48,49] and the Fukui[26] function, however, reveal a different story. Because of the presence of an Ag atom, the surface of the cluster shows two different types of reactive sites. In the next section, we

https://doi.org/10.1021/acscatal.1c02083
ACS Catal. 2021, 11, 11459−11468

have elaborated on how such active sites of a cluster can influence and control a redox reaction like the cross-coupling.

3.2. Alteration of Barrier Heights upon Silver Atom Doping. To investigate the catalytic performance of the Pd_{13} and $Pd_{12}Ag$ clusters, we have considered the SM cross-coupling[23,24] as a template redox reaction. The SM cross-coupling reaction is conventionally catalyzed by Pd(0)-based organometallic reagents, for example, $Pd(PPh_3)_4$ or tetrakis-(triphenylphosphine)palladium(0).[60] The 18e $Pd(PPh_3)_4$ complex actually acts as the precatalyst for the reaction. The real catalyst of the reaction is the 14e $Pd(PPh_3)_2$ complex, which is formed via the ligand dissociation of $Pd(PPh_3)_4$.[61] To benchmark the reaction parameters of the selected clusters toward the SM coupling, we have first computed the reaction pathway of biphenyl (Ph−Ph) synthesis from bromobenzene and phenylboronic acid on the $Pd(PPh_3)_2$ catalyst. Figure 4 shows the respective reaction pathway and the barrier heights for the important steps of SM coupling. The computed results are also included in Table 1 alongside the exothermicity (ΔH_r) and the changes in the Gibbs free energy (ΔG_r) for the reaction. As shown in Figure 4, we have followed the conventional reaction mechanism of the SM reaction as reported in the literature.[61−63] Thus, the whole reaction pathway of SM coupling is considered to be composed of three major steps, that is, (a) oxidative addition, (b) transmetallation, and (c) reductive elimination. The ligand substitution step between steps a and b is also shown. The structure of the pre-reaction complex (PRC) is shown as 1 in Figure 4, and the subsequent species are numbered (2 to 10) accordingly. The transition states are denoted with an asterisk (*) symbol. The PRC (1) is formed by the adsorption of the bromobenzene molecule on top of the Pd atom of the catalyst. The activation barriers for the three steps (Table 1 and Figure 4) are observed to be 0.62, 1.24, and 0.23 eV, respectively. According to the energetic span model (ESM),[40−45] the transition state and the preceding intermediate of the transmetallation step are observed to be the rate-determining states. The representative data are included in the Supporting Information (Figure S4). The ΔH_r and the ΔG_r values (at 298.15 K and 1 atm) are calculated as −4.47 and −4.33 eV, respectively.

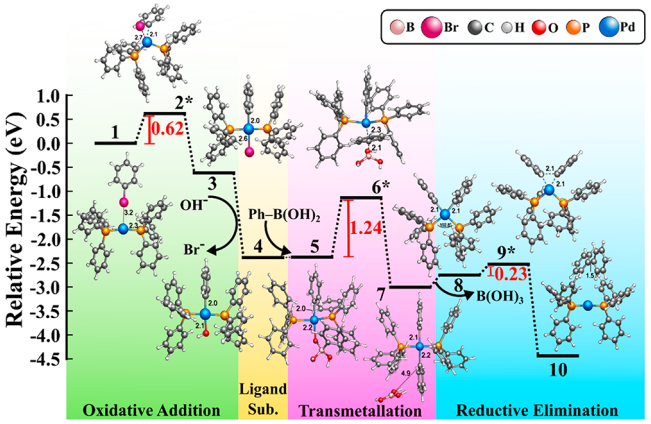

Figure 4. Calculated reaction pathway for the SM cross-coupling reaction of bromobenzene and phenylboronic acid on the $Pd(PPh_3)_2$ catalyst. The activation barriers of the three important steps are shown in eV. The transition states are marked by an asterisk (*) symbol.

To calculate the reaction pathway on both clusters, that is, Pd_{13} and $Pd_{12}Ag$, a similar catalytic cycle is considered, and a schematic is shown in Figure 5a ($R^1 = R^2 = Ph$). Because the reaction on the $Pd(PPh_3)_2$ catalyst proceeds on top of the Pd atom, a single atom on the surface of the cluster is chosen as the active site for the reaction. To dope the silver (Ag) atom on the surface, we have chosen three possible sites, as shown in Figure 5b. The first one is at the active site (site A). Additionally, two of the adjacent locations are chosen as the second (site B) and third (site C) sites, respectively. The location of site B and site C is chosen in such a way that site B resides near the R^1 fragment (originating from bromobenzene), whereas site C is located close to the R^2 fragment, which is derived from the phenylboronic acid. For convenience, the reaction is always considered to be occurring at the fixed active site as shown in Figure 5b, and only the dopant location is altered. According to our discussion in Section 3.1, doping an Ag atom on the surface makes nearby palladium sites susceptible to an electrophilic attack. Therefore, it is expected that doping the Ag atom either at site B or C will show a similar trend in the barrier heights because both sites are

Table 1. Activation Energies and the Thermodynamic Parameters of the Suzuki Cross-Coupling Reaction on $Pd(PPh_3)_2$, Pd_{13}, and $Pd_{12}Ag$ Clusters[a]

system	spin multiplicity ($M = 2S + 1$)	activation energy (eV)			ΔH_r (eV)	ΔG_r (eV)
		oxidative addition	transmetallation	reductive elimination		
$Pd(PPh_3)_2$	1 (GS)	0.62	1.24	0.23	−4.47	−4.33
	1	0.27	0.72	0.57	−4.33	−4.26
Pd_{13}	3(GS)	0.29	0.75	0.51	−4.30	−4.25
	5	0.21	0.70	0.55	−4.43	−4.24
	2	0.98	0.67	1.10	−4.46	−4.32
$Pd_{12}Ag$−A	4	1.00	0.64	1.07	−4.48	−4.25
	6(GS)	1.10	0.56	0.96	−4.41	−4.36
	2	0.10	0.72	0.36	−4.44	−4.29
$Pd_{12}Ag$−B	4	0.10	0.69	0.37	−4.38	−4.34
	6(GS)	0.07	0.72	0.25	−4.46	−4.26
	2	0.20	0.75	0.23	−4.28	−4.20
$Pd_{12}Ag$−C	4	0.17	0.75	0.26	−4.29	−4.21
	6(GS)	0.12	0.63	0.18	−4.38	−4.29

[a] ΔH_r = Exothermicity and ΔG_r = Changes in the Gibbs free energy of the reaction at 298.15 K and 1 atm.

https://doi.org/10.1021/acscatal.1c02083
ACS Catal. 2021, 11, 11459−11468

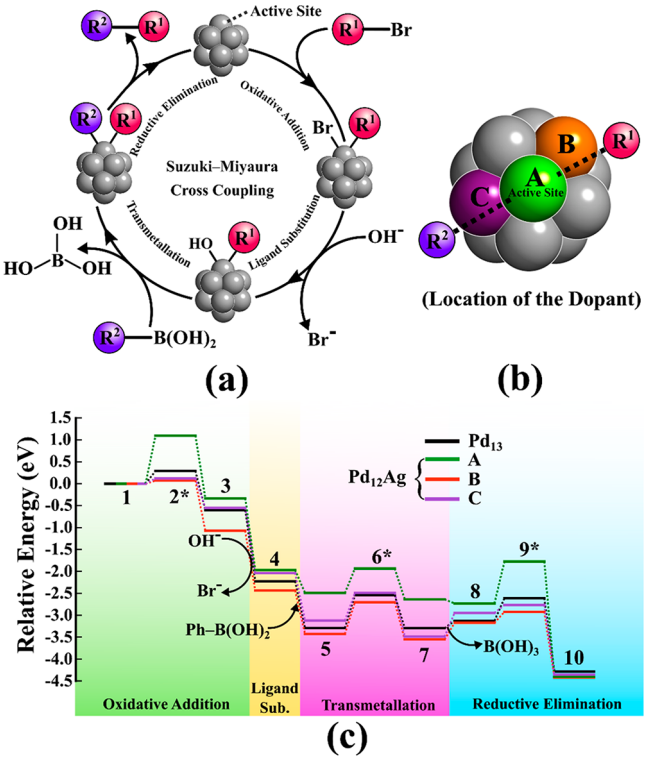

Figure 5. (a) Schematics of the SM coupling reaction on the active site of an icosahedral cluster. (b) Three chosen locations (A, B, and C) for the Ag dopant on the surface of the palladium cluster. (c) Reaction pathway of the SM coupling reaction on Pd_{13} and for all three cases (A, B, and C) of the $Pd_{12}Ag$ cluster. Only the pathway corresponding to the GS pre-reaction complex (PRC) is shown for each case. The transition states are marked by an asterisk (*) symbol.

adjacent to the active site. On the other hand, a reverse trend should be observed when the dopant atom is placed directly at the active site, that is, site A.

To validate our assumptions, we have calculated the reaction pathway of SM coupling for Pd_{13} and for the three (A, B, and C) conformers of the $Pd_{12}Ag$ clusters. Table 1 includes the summary of the calculated results. The structure of the PRC is observed to be similar to the $Pd(PPh_3)_2$ pathway, that is, the bromobenzene molecule is adsorbed on top of the active site. Because of the availability of a much larger surface area, the Ph terminal of the bromobenzene molecule has also interacted with the nearby atoms on the cluster. It was noticed that the GS spin multiplicity of the PRC differs from the GS multiplicity of Pd_{13} and $Pd_{12}Ag$ clusters. In all cases, the spin multiplicity of the GS PRC is calculated to be lower than the multiplicity of the global minima of both clusters. The relative energy ordering of the PRCs is provided in the Supporting Information (Table S5). The lowering of the spin multiplicity in the PRC can be attributed to the spin quenching because of the adsorption of the electron-rich Ph−Br molecule on the surface. The GS spin multiplicity of the PRC for the SM reaction on the Pd_{13} cluster is calculated to be a triplet (M = 3). On the contrary, for all three cases (A, B, and C) of the $Pd_{12}Ag$ cluster, the GS spin multiplicity of the PRC is observed to be 6. Because the barrier height generally shows a strong dependence on the spin state, we have calculated the full reaction pathway for two nearby spin states in addition to the pathway following the GS spin multiplicity of the PRCs. Thus, the barrier heights for M = 1, 3, and 5 are reported for Pd_{13}, whereas, in the case of the $Pd_{12}Ag$ cluster, the results for the M = 2, 4, and 6 are included (Table 1). Figure 5c shows the energy profile of the SM coupling on Pd_{13} and all three geometries (A, B, and C) of the $Pd_{12}Ag$ cluster. For simplicity, in Figure 5c, we have only shown the energy profile diagram following the GS spin multiplicity of the respective PRC in each case. The optimized structures of all the respective species in the reaction coordinate are included in Figures 6 and 7. The

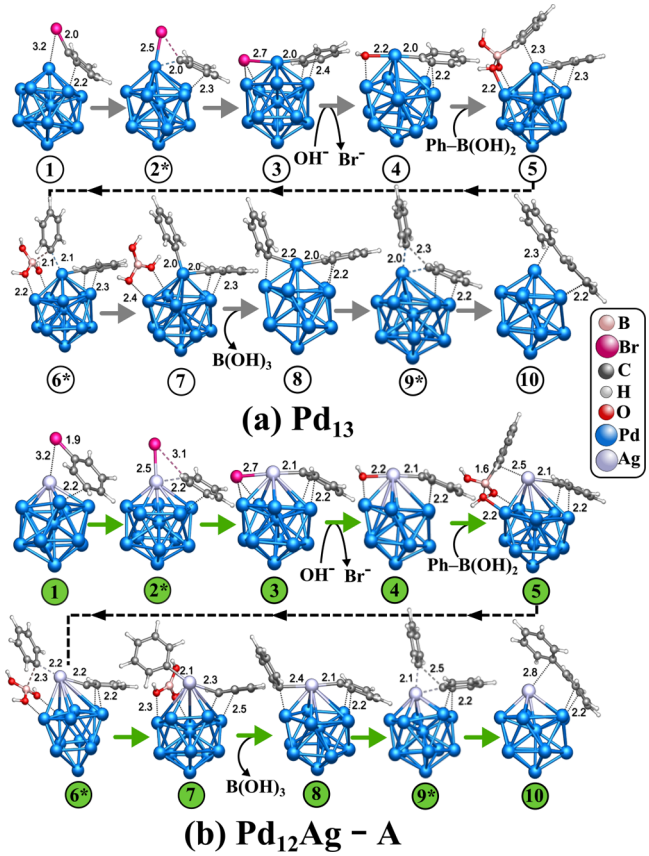

Figure 6. Optimized structures of the chemical species in the reaction coordinate of the SM cross-coupling reaction on (a) Pd_{13} and (b) $Pd_{12}Ag$-A clusters. Only the structures corresponding to the GS spin multiplicity of the PRC are shown. The transition states are marked by an asterisk (*) symbol.

optimized geometries obtained in other spin multiplicities are observed to be quite similar, and hence only the structures corresponding to the GS spin multiplicity of the PRC are provided herewith. Considering all three spin states (Table 1), the range of barrier heights of the oxidative addition (0.21−0.29 eV) and transmetallation (0.70−0.75 eV) steps is observed to be relatively lower on the Pd_{13} cluster compared to $Pd(PPh_3)_2$. In contrast, the barrier range for the reductive elimination (0.51−0.57 eV) is calculated to be higher. The activation barriers calculated for M = 3 (i.e., at the spin multiplicity of the GS PRC) are calculated as 0.29, 0.75, and 0.51 eV, respectively. The range of ΔH_r for the Pd_{13} cluster is within −4.30 to −4.43 eV, and the ΔG_r values are observed to be within −4.24 to −4.26 eV considering all three reported spin states. Because the rate constants often provide a direct way to compare the catalytic activity of the respective species, we have also calculated the rate constants[38,39] of the individual steps and TOFs[40−45] of the whole catalytic cycles for

https://doi.org/10.1021/acscatal.1c02083
ACS Catal. 2021, 11, 11459−11468

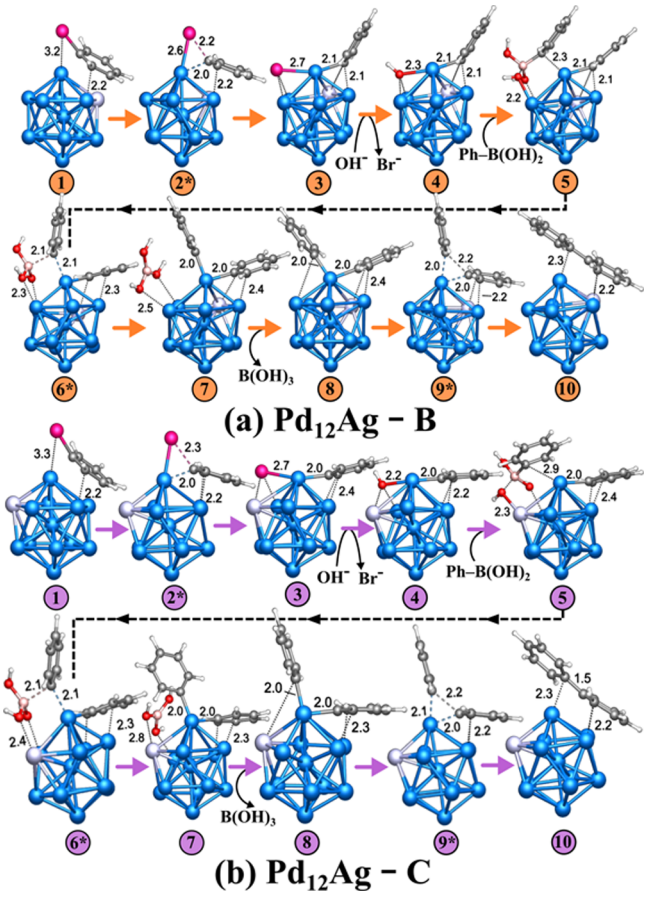

Figure 7. Optimized structures of the chemical species in the reaction coordinate of the SM cross-coupling reaction on (a) $Pd_{12}Ag$-B and (b) $Pd_{12}Ag$-C clusters. Only the structures corresponding to the GS spin multiplicity of the PRC are shown. The transition states are marked by an asterisk (*) symbol.

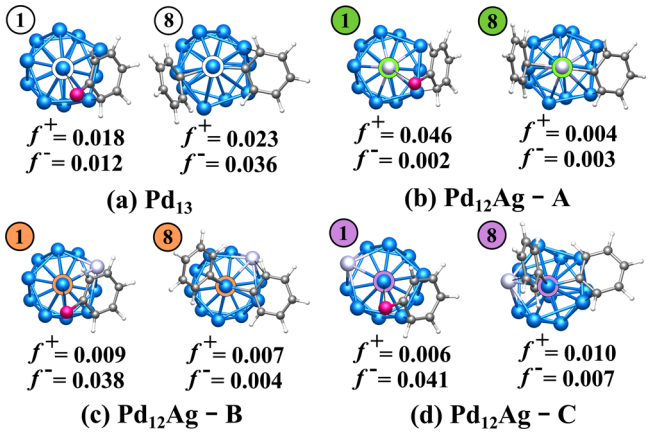

Figure 8. Values of the condensed Fukui (f^+ and f^-) indices at the respective active site of species 1 and 8 in the SM cross-coupling reaction pathway on (a) Pd_{13} and (b–d) $Pd_{12}Ag$ (A, B, and C) clusters.

comparison purposes. The results are included in Table S6 of the Supporting Information.

Among the three steps of the SM coupling, oxidative addition involves the dissociation of the C–X (X = halogen atom) bond on the active site. According to the MO theory,[61] in the oxidative addition step, the electron pair from the bonding orbital of the C–X bond is donated to the empty hybrid orbital of the metal. Simultaneously, the filled d orbital of the metal center donates an electron pair to the antibonding MO of the C–X bond, which results in the weakening of the bond and subsequent dissociation. Thus, the barrier height of the oxidative addition step largely depends on the electron-donating property of the metal. Because doping an Ag atom on the active site (site A) makes the site electron-deficient (Lewis acidic), it is expected that the activation barrier for oxidative addition will increase in this case. On the other hand, as shown earlier, if the Ag atom is placed on either B or C, the active site, which is now adjacent to the dopant Ag, will become susceptible to an electrophilic attack. Thus, a reduction in the barrier height is anticipated for both cases. Our calculated results (Table 1 and Figure 5c) indeed show the same. A significant increment in the first barrier was observed for all three spin states of A. In contrast, reduction of barrier heights of the oxidative addition was noticed for both B and C. To explain the trend, we have calculated the Fukui[25] indices (Figure 8) at the active site of each PRC (designated as 1 in Figures 5–8) for Pd_{13} and $Pd_{12}Ag$ (A, B, and C) clusters. The respective active site of 1 of A (Figure 8b) shows a significantly higher value of f^+ compared to f^- and further signifies that the active site, in this case, is unfavorable for an electrophilic attack. The computed barrier heights have also shown the same. On the contrary, for both B and C (Figure 8c,d), the active sites offer a reasonably higher f^- value than f^+, proving that these sites are highly susceptible to an electrophilic attack. For the GS pre-reaction complex of the Pd_{13} cluster (Figure 8a), the computed f^+ and f^- values of the active site are of similar magnitude, and the f^+ (0.018) value is marginally higher than f^-(0.012). Additionally, the f^- value is much lower compared to either B or C. These results revalidate our previous arguments and provide the reasoning behind the computed lower first barrier for B and C as compared to the pristine Pd_{13} from a reactivity perspective.

The reductive elimination step is conceptually the opposite of oxidative addition.[61] In this step, the catalyst retains the electron pair back, which was donated to the reactants in the oxidative addition step. The calculated trend of the barrier heights for the reductive elimination step has remained the same as the oxidative addition. Thus, compared to Pd_{13}, a reduction of barrier heights is noticed for both B and C, whereas a relative increment is observed for A. This observation can also be explained in terms of the Fukui indices as before. We have included the value of f^+ and f^- for intermediate 8 for Pd_{13} and $Pd_{12}Ag$ (A, B, and C) in Figure 8. The intermediate 8 is the structure in the reaction coordinate that precedes the transition state (9* in Figures 5–7) of the reductive elimination. It can be seen from Figure 8c,d that after donating the charge in the oxidative addition step of B and C isomers of the $Pd_{12}Ag$ cluster, the active sites have now become marginally more susceptible to nucleophilic attack. Thus, although both f^+ and f^- values are quite low and the difference between them is small, a marginally higher f^+ value for B and C still partially favors the reductive elimination step. For Pd_{13}, (Figure 8a), although both f^+ and f^- values are comparatively higher compared to B or C, the f^- value now predominates over the f^+, which results in a relatively higher barrier (compared to B or C) for the reductive elimination step as obtained for Pd_{13} (Table 1). The situation for A at the reductive elimination step is interesting. As depicted in Figure 8b, the active site of the intermediate 8 shows a nearly equal

https://doi.org/10.1021/acscatal.1c02083
ACS Catal. 2021, 11, 11459–11468

value of f^+ and f^-. In addition, both values are also very low. This demonstrates that at this stage, the Ag site has become almost passive toward either electrophilic or nucleophilic attack, which is reflected in the higher barriers of the reductive elimination step for A.

At this point, it has become quite evident that doping the Ag atom at A increases the barrier heights of both oxidative addition and reductive elimination, whereas an opposite trend is noticed for B and C. It is possible that one might obtain different barrier heights by incorporating a better functional or by including self-interaction corrections.[64,65] However, it can be expected that the relative trend will remain the same as seen for the HOMO−LUMO gap, which is discussed in Section 3.1. The reverse trend in the computed barrier heights of the redox steps provides a way to control the reaction by altering the type of the active site (Pd or Ag). Such techniques can be useful to prevent unwanted side reactions or to alter the conversion rate between two competitive reactions. Additionally, one cannot ignore the intriguing possibility of switching the rate-determining states for a catalytic cycle. For example, according to the ESM[40−45] (Figure S4 in the Supporting Information), the rate-determining states of the $Pd_{12}Ag$-A pathway belong to oxidative addition, whereas for the rest of the systems, the states related to the transmetallation are identified as rate-determining. Apart from that, as shown in Table 1, the trend in the barrier heights is independent with respect to the spin state, which suggests that the alteration of barrier heights is definitely a surface-related phenomenon and the electronic structure of the cluster has a smaller effect. Thus, the alteration will happen even in higher spin states and is not restricted only to the GS. This is an additional advantage because, in most clusters, several different spin states lie very close in energy to the GS.

Finally, it is also important to discuss the transmetallation step. In both the B and C pathways (considering all the reported spin states in Table 1), the barriers for transmetallation have remained almost similar to Pd_{13} (0.70−0.75 eV). Only for A, a minor reduction is noticed in the overall range (0.56−0.67 eV). Because in the transmetallation step, the oxidation state of the active site remains unaltered, it is expected that the electrophilicity or nucleophilicity of the active site will have a minor influence on the transmetallation process. It is proven in the past studies that the barrier heights of transmetallation in the SM reaction depends on the polarity difference of the following two bonds, the B−C bond, which is breaking, and the metal−carbon bond, which is forming.[66,67] Because the metal atom (Pd) is not changing in B or C, no reasonable change in the barrier height is noticed for those two cases compared to Pd_{13}. Only for A, where the Ag atom is placed at the active site, is there a polarity alteration of the metal-carbon bond, which results in the observed minor lowering of the transmetallation barrier.

4. CONCLUSIONS

The inclusion of a silver atom on a vertex of icosahedral Pd_{13} clusters alters the charge distribution on the surface of the cluster. The electronic structure of the clusters was observed to remain mostly unchanged, especially near the valence region. In contrast, the property of the surface has altered significantly, which is confirmed by the overall charge distribution,[47,50,51,55] average local ionization energy,[48,49] and the Fukui[25−27] function. Thus, the $Pd_{12}Ag$ cluster shows two different types of reactive sites. Our calculation shows that the Pd atoms in the vicinity of the dopant Ag atom are effective in reducing the computed barrier heights of the redox steps of Suzuki coupling. On the other hand, an opposite trend is noticed when the dopant Ag atom is chosen as the active site. A comparison of the calculated barrier shows that, if the Pd sites are chosen as the active site, the $Pd_{12}Ag$ cluster can theoretically act as a better catalyst for the redox steps than the pristine Pd_{13} cluster and $Pd(PPh_3)_2$ catalyst. Additionally, the site dependence of the cluster can potentially be useful as an effective tool to control the barrier heights of the redox steps of cross-coupling or analogous reactions. The computed reactivity descriptors show close agreement with the calculated barrier heights, which indicates that for these two reported clusters, that is, Pd_{13} and $Pd_{12}Ag$, the observed trends are theoretically predictable and not random. As an added advantage, the relative trend in the barrier heights is also found to be spin-independent for both clusters. However, it is important to mention that all of the observations reported herewith are based on only the Pd_{13} and $Pd_{12}Ag$ clusters, and some of them may not be universally applicable to other sizes. Additionally, from an experimental perspective, one might face some challenges in synthesizing such systems, to dope the Ag atom at a specific location or to place the reagents at the desired site. Despite these, from the reported results in this paper, it can be said with certainty that the $Pd_{12}Ag$ cluster is indeed an interesting system and if the same or similar bimetallic Pd_xAg_y clusters can be synthesized experimentally, they can provide a superior and cheaper alternative as the catalyst for the Suzuki cross-coupling[23,24] reaction.

■ ASSOCIATED CONTENT

Supporting Information

The Supporting Information is available free of charge at https://pubs.acs.org/doi/10.1021/acscatal.1c02083.

Relative energies, Mulliken charges, spin density, ALIE, rate constants, TOFs, and other data (PDF)

■ AUTHOR INFORMATION

Corresponding Author

Shiv N. Khanna − *Department of Physics, Virginia Commonwealth University, Richmond, Virginia 23284-2000, United States;* orcid.org/0000-0002-9797-1289; Email: Snkhanna@vcu.edu

Authors

Turbasu Sengupta − *Department of Physics, Virginia Commonwealth University, Richmond, Virginia 23284-2000, United States;* orcid.org/0000-0003-3562-4414

Dinesh Bista − *Department of Physics, Virginia Commonwealth University, Richmond, Virginia 23284-2000, United States;* orcid.org/0000-0002-5168-0881

Complete contact information is available at: https://pubs.acs.org/10.1021/acscatal.1c02083

Author Contributions

T.S. and D.B. have performed all the calculations. This paper was written by S.N.K. and T.S. All authors have discussed the results.

Notes

The authors declare no competing financial interest.

■ ACKNOWLEDGMENTS

We thank the National Science Foundation (CHE-1900094) for the support to this work.

■ REFERENCES

(1) wassel, A. R.; el-Naggar, M. E.; Shoueir, K. Recent Advances in Polymer/Metal/Metal Oxide Hybrid Nanostructures for Catalytic Applications. *J. Environ. Chem. Eng.* **2020**, *8*, No. 104175.
(2) Shifrina, Z. B.; Matveeva, V. G.; Bronstein, L. M. Role of Polymer Structures in Catalysis by Transition Metal and Metal Oxide Nanoparticle Composites. *Chem. Rev.* **2020**, *120*, 1350−1396.
(3) Pomogailo, A. D. *Catalysis by Polymer-Immobilized Metal Complexes*; CRC Press, 2020.
(4) Yadav, R. K.; Oh, G. H.; Park, N.-J.; Kumar, A.; Kong, K.; Baeg, J.-O. Highly Selective Solar-Driven Methanol from CO_2 by a Photocatalyst/Biocatalyst Integrated System. *J. Am. Chem. Soc.* **2014**, *136*, 16728−16731.
(5) Amao, Y.; Kataoka, R. Methanol Production from CO_2 with the Hybrid System of Biocatalyst and Organo-Photocatalyst. *Catal. Today* **2018**, *307*, 243−247.
(6) Son, E. J.; Lee, Y. W.; Ko, J. W.; Park, C. B. Amorphous Carbon Nitride as a Robust Photocatalyst for Biocatalytic Solar-to-Chemical Conversion. *ACS Sustainable Chem. Eng.* **2019**, *7*, 2545−2552.
(7) Attanayake, N. H.; Banjade, H. R.; Thenuwara, A. C.; Anasori, B.; Yan, Q.; Strongin, D. R. Electrocatalytic CO_2 reduction on earth abundant 2D Mo_2C and Ti_3C_2MXenes. *Chem. Commun.* **2021**, *57*, 1675−1678.
(8) Heiz, U.; Bullock, E. L. Fundamental Aspects of Catalysis on Supported Metal Clusters. *J. Mater. Chem.* **2004**, *14*, 564−577.
(9) Gates, B. C. Supported Metal Cluster Catalysts. *J. Mol. Catal. A: Chem.* **2000**, *163*, 55−65.
(10) Alexeev, O. S.; Gates, B. C. Supported Bimetallic Cluster Catalysts. *Ind. Eng. Chem. Res.* **2003**, *42*, 1571−1587.
(11) Gates, B. C. Supported Metal Clusters: Synthesis, Structure, and Catalysis. *Chem. Rev.* **1995**, *95*, 511−522.
(12) Diederich, F.; Stang, P. J. *Metal-Catalyzed Cross-Coupling Reactions*; John Wiley & Sons, 2008.
(13) Kohei, T.; Miyaura, N. Introduction to Cross-Coupling Reactions. In *Cross-Coupling Reactions*; Springer, 2002; pp. 1−9.
(14) Miyaura, N.; Buchwald, S. L. *Cross-Coupling Reactions: A Practical Guide*; Springer, 2002; Vol. *219*.
(15) Luo, Z.; Khanna, S. N. Carbon-Carbon Cross-Coupling Reactions. In *Metal Clusters and Their Reactivity*; Springer, 2020; pp. 143−162.
(16) Yang, Y.; Reber, A. C.; Gilliland, S. E., III; Castano, C. E.; Gupton, B. F.; Khanna, S. N. More than Just a Support: Graphene as a Solid-State Ligand for Palladium-Catalyzed Cross-Coupling Reactions. *J. Catal.* **2018**, *360*, 20−26.
(17) Ibrahim, A. A.; Lin, A.; Adly, M. S.; El-Shall, M. S. Enhancement of the Catalytic Activity of Pd Nanoparticles in Suzuki Coupling by Partial Functionalization of the Reduced Graphene Oxide Support with *p*-Phenylenediamine and Benzidine. *J. Catal.* **2020**, *385*, 194−203.
(18) Shieh, W.-C.; Shekhar, R.; Blacklock, T.; Tedesco, A. A Simple, Recyclable, Polymer-Supported Palladium Catalyst for Suzuki Coupling—an Effective Way To Minimize Palladium Contamination. *Synth. Commun.* **2002**, *32*, 1059−1067.
(19) Pagliaro, M.; Pandarus, V.; Ciriminna, R.; Béland, F.; Demma Carà, P. Heterogeneous versus Homogeneous Palladium Catalysts for Cross-Coupling Reactions. *ChemCatChem* **2012**, *4*, 432−445.
(20) Peric, T.; Jakovljevic, V. Lj.; Zivkovic, V.; Krkeljic, J.; Petrovic, Z. D.; Simijonovic, D.; Novokmet, S.; Djuric, D. M.; Jankovic, S. M. Toxic Effects of Palladium Compounds on the Isolated Rat Heart. *Med. Chem.* **2012**, *8*, 9−13.
(21) Kielhorn, J.; Melber, C.; Keller, D.; Mangelsdorf, I. Palladium—a Review of Exposure and Effects to Human Health. *Int. J. Hyg. Environ. Health* **2002**, *205*, 417−432.
(22) Yang, Y.; Castano, C. E.; Gupton, B. F.; Reber, A. C.; Khanna, S. N. A Fundamental Analysis of Enhanced Cross-Coupling Catalytic Activity for Palladium Clusters on Graphene Supports. *Nanoscale* **2016**, *8*, 19564−19572.
(23) Miyaura, N.; Suzuki, A. Palladium-Catalyzed Cross-Coupling Reactions of Organoboron Compounds. *Chem. Rev.* **1995**, *95*, 2457−2483.
(24) Suzuki, A. Cross-Coupling Reactions via Organoboranes. *J. Organomet. Chem.* **2002**, *653*, 83−90.
(25) Martínez, J. Local Reactivity Descriptors from Degenerate Frontier Molecular Orbitals. *Chem. Phys. Lett.* **2009**, *478*, 310−322.
(26) Parr, R. G.; Yang, W. Density Functional Approach to the Frontier-Electron Theory of Chemical Reactivity. *J. Am. Chem. Soc.* **1984**, *106*, 4049−4050.
(27) Li, Y.; Evans, J. N. S. The Fukui Function: A Key Concept Linking Frontier Molecular Orbital Theory and the Hard-Soft-Acid-Base Principle. *J. Am. Chem. Soc.* **1995**, *117*, 7756−7759.
(28) te Velde, G.; Bickelhaupt, F. M.; Baerends, E. J.; Fonseca Guerra, C.; van Gisbergen, S. J. A.; Snijders, J. G.; Ziegler, T. Chemistry with ADF. *J. Comput. Chem.* **2001**, *22*, 931−967.
(29) Perdew, J. P.; Burke, K.; Ernzerhof, M. Generalized Gradient Approximation Made Simple. *Phys. Rev. Lett.* **1996**, *77*, 3865−3868.
(30) Van Lenthe, E.; Baerends, E. J. Optimized Slater-Type Basis Sets for the Elements 1−118. *J. Comput. Chem.* **2003**, *24*, 1142−1156.
(31) Chong, D. P.; Van Lenthe, E.; Van Gisbergen, S.; Baerends, E. J. Even-Tempered Slater-Type Orbitals Revisited: From Hydrogen to Krypton. *J. Comput. Chem.* **2004**, *25*, 1030−1036.
(32) van Lenthe, E.; Snijders, J. G.; Baerends, E. J. The Zero-order Regular Approximation for Relativistic Effects: The Effect of Spin−Orbit Coupling in Closed Shell Molecules. *J. Chem. Phys.* **1996**, *105*, 6505−6516.
(33) Van Lenthe, E.; Ehlers, A.; Baerends, E.-J. Geometry Optimizations in the Zero Order Regular Approximation for Relativistic Effects. *J. Chem. Phys.* **1999**, *110*, 8943−8953.
(34) Fan, L.; Ziegler, T. Optimization of Molecular Structures by Self-Consistent and Nonlocal Density-Functional Theory. *J. Chem. Phys.* **1991**, *95*, 7401−7408.
(35) Bérces, A.; Dickson, R. M.; Fan, L.; Jacobsen, H.; Swerhone, D.; Ziegler, T. An Implementation of the Coupled Perturbed Kohn-Sham Equations: Perturbation Due to Nuclear Displacements. *Comput. Phys. Commun.* **1997**, *100*, 247−262.
(36) Jacobsen, H.; Bérces, A.; Swerhone, D. P.; Ziegler, T. Analytic Second Derivatives of Molecular Energies: A Density Functional Implementation. *Comput. Phys. Commun.* **1997**, *100*, 263−276.
(37) Deng, L.; Ziegler, T. The Determination of Intrinsic Reaction Coordinates by Density Functional Theory. *Int. J. Quantum Chem.* **1994**, *52*, 731−765.
(38) Eyring, H. The Activated Complex and the Absolute Rate of Chemical Reactions. *Chem. Rev.* **1935**, *17*, 65−77.
(39) Evans, M. G.; Polanyi, M. Some applications of the transition state method to the calculation of reaction velocities, especially in solution. *Trans. Faraday Soc.* **1935**, *31*, 875−894.
(40) Kozuch, S. A Refinement of Everyday Thinking: The Energetic Span Model for Kinetic Assessment of Catalytic Cycles. *Wiley Interdiscip. Rev. Comput. Mol. Sci.* **2012**, *2*, 795−815.
(41) Kozuch, S.; Shaik, S. How to Conceptualize Catalytic Cycles? The Energetic Span Model. *Acc. Chem. Res.* **2011**, *44*, 101−110.
(42) Kozuch, S.; Shaik, S. A Combined Kinetic-Quantum Mechanical Model for Assessment of Catalytic Cycles: Application to Cross-Coupling and Heck Reactions. *J. Am. Chem. Soc.* **2006**, *128*, 3355−3365.
(43) Kozuch, S.; Shaik, S. Kinetic-Quantum Chemical Model for Catalytic Cycles: The Haber-Bosch Process and the Effect of Reagent Concentration. *J. Phys. Chem. A* **2008**, *112*, 6032−6041.
(44) Kozuch, S.; Martin, J. M. L. What Makes for a Bad Catalytic Cycle? A Theoretical Study on the Suzuki-Miyaura Reaction within the Energetic Span Model. *ACS Catal.* **2011**, *1*, 246−253.

https://doi.org/10.1021/acscatal.1c02083
ACS Catal. 2021, 11, 11459−11468

(45) Kozuch, S.; Lee, S. E.; Shaik, S. Theoretical Analysis of the Catalytic Cycle of a Nickel Cross-Coupling Process: Application of the Energetic Span Model. *Organometallics* **2009**, *28*, 1303−1308.
(46) Bader, R. F. Atoms in Molecules. *Acc. Chem. Res.* **1985**, *18*, 9−15.
(47) Bultinck, P.; Van Alsenoy, C.; Ayers, P. W.; Carbó-Dorca, R. Critical Analysis and Extension of the Hirshfeld Atoms in Molecules. *J. Chem. Phys.* **2007**, *126*, 144111.
(48) Politzer, P.; Murray, J. S.; Bulat, F. A. Average Local Ionization Energy: A Review. *J. Mol. Model.* **2010**, *16*, 1731−1742.
(49) Politzer, P.; Murray, J. S. The Average Local Ionization Energy: Concepts and Applications. In *Theoretical and Computational Chemistry*; Elsevier, 2007; Vol. *19*, pp. 119−137.
(50) Frisch, M.; Trucks, G. W.; Schlegel, H. B.; Scuseria, G. E.; Robb, M. A.; Cheeseman, J. R.; Scalmani, G.; Barone, V.; Mennucci, B.; Petersson, Ga. *Gaussian 09, Revision D. 01*; Gaussian, Inc., Wallingford, CT, 2009.
(51) Lu, T.; Chen, F. Multiwfn: A Multifunctional Wavefunction Analyzer. *J. Comput. Chem.* **2012**, *33*, 580−592.
(52) Weigend, F.; Ahlrichs, R. Balanced Basis Sets of Split Valence, Triple Zeta Valence and Quadruple Zeta Valence Quality for H to Rn: Design and Assessment of Accuracy. *Phys. Chem. Chem. Phys.* **2005**, *7*, 3297−3305.
(53) Weigend, F. Accurate Coulomb-Fitting Basis Sets for H to Rn. *Phys. Chem. Chem. Phys.* **2006**, *8*, 1057−1065.
(54) Gracia-Espino, E.; Hu, G.; Shchukarev, A.; Wågberg, T. Understanding the Interface of Six-Shell Cuboctahedral and Icosahedral Palladium Clusters on Reduced Graphene Oxide: Experimental and Theoretical Study. *J. Am. Chem. Soc.* **2014**, *136*, 6626−6633.
(55) Fonseca Guerra, C.; Handgraaf, J.-W.; Baerends, E. J.; Bickelhaupt, F. M. Voronoi Deformation Density (VDD) Charges: Assessment of the Mulliken, Bader, Hirshfeld, Weinhold, and VDD Methods for Charge Analysis. *J. Comput. Chem.* **2004**, *25*, 189−210.
(56) Philips, J. J.; Hudspeth, M. A.; Browne, P. M., Jr.; Peralta, J. E. Basis Set Dependence of Atomic Spin Populations. *Chem. Phys. Lett.* **2010**, *495*, 146−150.
(57) Kar, T.; Sannigrahi, A. B. Effect of Basis Set on Mulliken and Löwdin Atomic Charges, Bond Orders and Valencies of Some Polar Molecules. *J. Mol. Struct. Theochem.* **1988**, *165*, 47−54.
(58) Mulliken, R. S. Electronic Population Analysis on LCAO−MO Molecular Wave Functions. I. *J. Chem. Phys.* **1955**, *23*, 1833−1840.
(59) Benítez, J. I.; Flores, R.; Castro, M. Theoretical Study for the Adsorption of CO on Neutral and Charged Pd_{13} Clusters. *Can. J. Chem.* **2013**, *91*, 1033−1042.
(60) Coulson, D.-R.; Satek, L. C.; Grim, S. O. Tetrakis (Triphenylphosphine) Palladium (0). *Inorg. Synth.* **1972**, *13*, 121−124.
(61) Loudon, M.; Parise, J. *Organic Chemistry*; Macmillan Learning, 2015.
(62) Lennox, A. J. J.; Lloyd-Jones, G. C. Selection of Boron Reagents for Suzuki−Miyaura Coupling. *Chem. Soc. Rev.* **2014**, *43*, 412−443.
(63) Zhang, B.; Song, J.; Liu, H.; Shi, J.; Ma, J.; Fan, H.; Wang, W.; Zhang, P.; Han, B. Acceleration of Suzuki Coupling Reactions by Abundant and Non-Toxic Salt Particles. *Green Chem.* **2014**, *16*, 1198−1201.
(64) Perdew, J. P.; Ruzsinszky, A.; Sun, J.; Pederson, M. R. Paradox of Self-Interaction Correction: How Can Anything so Right Be so Wrong? *Adv. At., Mol., Opt. Phys.* **2015**, *64*, 1−14.
(65) Zope, R. R.; Yamamoto, Y.; Diaz, C. M.; Baruah, T.; Peralta, J. E.; Jackson, K. A.; Santra, B.; Perdew, J. P. A Step in the Direction of Resolving the Paradox of Perdew-Zunger Self-Interaction Correction. *J. Chem. Phys.* **2019**, *151*, 214108.
(66) Rasmussen, S. C. Transmetalation: A Fundamental Organometallic Reaction Critical to Synthesis and Catalysis. *ChemTexts* **2021**, *7*, 1.
(67) Mudi, S. Y.; Usman, M. T.; Ibrahim, S. Clinical and Industrial Application of Organometallic Compounds and Complexes: A Review. *Am. J. Chem. Appl.* **2015**, *2*, 151−158.

https://doi.org/10.1021/acscatal.1c02083
ACS Catal. 2021, 11, 11459−11468